Nonlinear bubble dynamics

Andrea Prosperetti
Department of Mechanical Engineering, The Johns Hopkins University, Baltimore, Maryland 21218

Lawrence A. Crum
National Center for Physical Acoustics, P.O. Box 847, University, Mississippi 38677

Kerry W. Commander
Physical Acoustics Branch, Naval Coastal Systems Center, Code 4120, Panama City, Florida 32407

The standard approach to the analysis of the pulsations of a driven gas bubble is to assume that the pressure within the bubble follows a polytropic relation of the form $p = p_0(R_0/R)^{3\kappa}$, where p is the pressure within the bubble, R is the radius, κ is the polytropic exponent, and the subscript zero indicates equilibrium values. For nonlinear oscillations of the gas bubble, however, this approximation has several limitations and needs to be reconsidered. A new formulation of the dynamics of bubble oscillations is presented in which the internal pressure is obtained numerically and the polytropic approximation is no longer required. Several comparisons are given of the two formulations, which describe in some detail the limitations of the polytropic approximation.

INTRODUCTION

The dynamics of a gas bubble in a liquid is strongly dependent on the pressure of the gas contained in it. In principle, this quantity must be determined from the solution of the conservation equations of continuum mechanics inside and outside the bubble joined together by suitable boundary conditions at the bubble interface. This task is very complex and can only be carried out analytically for small-amplitude motion in which the equations can be linearized (see, for example, Refs. 1–4). For large-amplitude motion, it is customary in the literature to make use of a polytropic relation of the form

$$p = p_0 (R_0/R)^{3\kappa}, \tag{1}$$

where p is the pressure of the gas in the bubble, R is the radius, κ is the polytropic index, and the subscript zero indicates equilibrium values. This relation, with $\kappa = 1$, had already been used by Minnaert[5] in his calculation of the natural frequency of an oscillating bubble in 1933, but entered bubble-dynamics literature explictly with the pioneering numerical studies of forced large-amplitude oscillations carried out by Noltingk and Neppiras[6] in the early 1950s. After that, it has been used by virtually every writer on the subject such as Flynn,[7] Apfel,[8] Lauterborn,[9] Akulichev,[10] and many others.[11–13]

In spite of its appealing simplicity, the use of Eq. (1) poses many problems. In the first place, the polytropic index can range in the interval from 1 (isothermal) to the ratio of specific heats γ (adiabatic), and appropriate criteria for the proper choice are available only for the small-amplitude linear case. Further, it is at present unknown how realistic this

relation is when the linear value of κ is used in the nonlinear regime. Second, if p is given by (1), $p\,dv$ (where v is the volume of the bubble) is a perfect differential, and its integral over a cycle vanishes. As a consequence, use of (1) results in no energy loss associated with the heating and cooling of the gas. This fact is very unfortunate since it is known from the linear studies that this thermal damping is, in fact, the dominant form of energy absorption over a wide range of physical conditions. As a partial remedy, it was suggested in Ref. 12 that the liquid viscosity could be artificially augmented by an amount chosen in such a way that the correct damping would result in the linear case. This prescription has recently been put to an experimental test[14] and has been found to result in a large overestimate of the damping affecting the nonlinear oscillations in the region of the first nonlinear resonance. On the basis of these considerations, it must be concluded that Eq. (1) is not adequate for a precise theoretical analysis of bubble dynamics. Of particular concern is the application of (1) to the study of the chaotic regime of forced oscillations,[15] which is known to be strongly influenced by the details of energy dissipation.

In an attempt to go beyond (1), Flynn presented a mathematical formulation which reduced the exact set of partial differential equations expressing the conservation laws in the gas to a system of ordinary differential equations.[16] This result was obtained at the price of a number of approximations the most notable of which, that of spatially uniform pressure distribution in the bubble, is also adopted in this article. Flynn's formulation, however, is far from simple and, probably for this reason, has not been widely used.

The mathematical formulation to be presented here is simpler and more precise. For a perfect gas with spatially uniform pressure, the continuity and energy equations can

be combined to obtain an exact expression for the velocity field in terms of the temperature gradient. In this way, the problem is reduced to a nonlinear partial differential equation for the temperature field and to an ordinary differential equation for the internal pressure. A straightforward numerical technique for the treatment of these equations is described in the Appendix, and several numerical results are included for the purpose of illustrating the method and demonstrating the limited accuracy of the polytropic approximation. Further numerical and analytical results will be presented in forthcoming publications.

The main approximations contained in the present article are: (a) The pressure is spatially uniform in the bubble; (b) the gas is perfect; (c) the bubble maintains a spherical shape; (d) the bubble wall temperature remains unperturbed; and (e) the effects of the vapor contained in the bubble are negligible.

Assumptions (d) and (e) enable us to disregard the energy equation in the liquid and the gas–vapor diffusion equation in the bubble. They are not inherent to our approach, which can be generalized to dispense with them. In the order-of-magnitude analysis given in Sec. I, it will be shown that both assumptions are reasonable for sufficiently cold liquids, and, in particular, for water up to temperatures of the order of 50 °C. The first two assumptions are instead inherent to the present approach. The first one requires the Mach number of the bubble wall motion, calculated with respect to the gas speed of sound, to be small. Therefore, the present theory cannot be applied to very violent collapse cases, for which no simplified formulation is available short of the exact conservation laws. The second, third, and fourth assumptions are also likely to break down in the conditions of extreme gas temperature and pressure prevailing near the end of violent collapses, be they caused by large-amplitude acoustic driving or by the recovery of the ambient pressure typical of flow cavitation.

In summary, our formulation should be of value in a variety of situations involving free and forced motion in a relatively cold liquid, provided that the velocity of the bubble interface remain relatively small with respect to the speed of sound in the gas. This limitation is actually less stringent than it might appear since reference is made here to the instantaneous value of the speed of sound during the motion which, near the instants of time at which the minimum radius is attained, can be several times larger than that in undisturbed conditions. In other situations, our results can at least be expected to be superior to those obtained by use of (1).

In conclusion, we mention a work by Hickling,[17] which is the only study we are aware of to attempt a numerical solution of the complete set of conservation equations in a collapsing bubble. Compared to Hickling's approach, our formulation has the advantage of considerably greater simplicity and similar accuracy in its domain of applicability.

After the completion of this study, some work by Nigmatulin and co-workers came to our attention in which the assumption of uniform internal pressure is also used in a similar way.[18–20] The derivation of the model in this article is somewhat different, and the problems studied unrelated to those considered by the Russian authors.

I. MATHEMATICAL FORMULATION

We propose to study the thermomechanical behavior of the gas contained in a bubble in spherically symmetric motion. The diffusion of the gas in and out of the bubble has significant dynamical effects only at very low ambient pressures, when the small quantity of gas diffusing into the liquid is an appreciable fraction of the total amount of gas contained in the bubble.[21] This effect, however, can be ignored at higher pressures. A further consequence of diffusion manifests itself over time scales much longer than that associated with the typical oscillatory period of bubble motion. This process which, in the case of an oscillating bubble, is termed rectified diffusion,[22–24] results in a very slow change of parameters such as the equilibrium bubble radius and the total gas contents of the bubble, and again has negligible dynamical consequences. Accordingly, we shall disregard diffusion altogether and assume the bubble boundary to be impervious to the gas. The partial pressure of the liquid vapor is assumed to be much smaller than the gas pressure, and the effect of the vapor present in the bubble is also disregarded. This point will be discussed further after Eq. (18) below.

If ρ, p, u, and τ denote the density, pressure, radial velocity, and viscous stress tensor of the gas, the momentum equation is

$$\rho\left(\frac{\partial u}{\partial t} + u\,\frac{\partial u}{\partial r}\right) + \frac{\partial p}{\partial r} = \nabla \cdot \tau, \qquad (2)$$

where the point $r = 0$ corresponds to the bubble center. The boundary condition on the velocity is

$$u(r = R,t) = \dot{R}, \qquad (3)$$

where $R(t)$ is the instantaneous bubble radius and $\dot{R} = dR/dt$ is the velocity of the bubble wall. From a consideration of (2), it is easy to convince oneself that the pressure in the bubble may be assumed to be spatially uniform in many cases of practical interest. Indeed, from (3), we have the estimate $u \sim \dot{R}$ for the order of magnitude of the velocity of the gas. If Δp is the maximum pressure difference in the bubble, balancing $\partial p/\partial r \sim \Delta p/R$ with $\rho u\,\partial u/\partial r \sim \rho\dot{R}^2/R$, we have the estimate

$$\Delta p/p \sim \rho\dot{R}^2/p. \qquad (4)$$

For a gas, p/ρ is of the order of the square of the speed of sound and, therefore, $\Delta p/p$ is predicted to be of the order of the square of the Mach number M_B of the bubble wall. Similarly, balancing $\partial p/\partial r$ with $\rho\,\partial u/\partial t \sim \rho\dot{R}/t_0$, where t_0 is a characteristic time, leads to

$$\Delta p/p \sim \rho\,R\dot{R}/pt_0. \qquad (5)$$

The quantity $(p/\rho)^{1/2}t_0$ too can be identified with a characteristic wavelength λ_G of the pressure perturbations in the gas and, bringing together the preceding results, we may write

$$\Delta p/p = O(M_B\,R/\lambda_G, M_B^2). \qquad (6)$$

Typically, both R/λ_G and M_B are small. For example, the resonance frequency ω_0 of a bubble in a liquid, with the neglect of surface tension and thermal effects, is approximately

$$\omega_0 = (3\gamma p_\infty/\rho_L R_0^2)^{1/2}, \qquad (7)$$

where ρ_L is the liquid density and p_∞ is the undisturbed

pressure. If we set $\lambda_G \sim 2\pi(\gamma p_\infty/\rho)^{1/2}/\omega_0$, we find

$$R/\lambda_G \sim (1/2\pi)(\rho/\rho_L)^{1/2}, \qquad (8)$$

which for air and water at 1 atm is less than 10^{-2}. The same estimate holds for the Mach number if $\dot{R}$ is taken to be of the order $\omega_0 R_0$. In some cases, this estimate may not be accurate since the bubble wall velocity can be large during the collapse phase of the bubble motion, but (6) still suggests that taking the internal pressure to be a function of time only is an approximation with a quite useful range of validity. As for the viscous stresses, we may estimate the magnitude of their contribution to the momentum equation to be $\nabla \cdot \tau \sim \mu \dot{R}/R^2$, where μ is the viscosity of the gas, from which we get a pressure difference in the bubble of the order

$$\Delta p/p \sim \mu \dot{R}/pR, \qquad (9)$$

which is quite negligible in all circumstances.

The preceding analysis enables us to drop the momentum equation (2), substituting for it the statement

$$p = p(t). \qquad (10)$$

The remaining equations express the conservation of mass,

$$\frac{d\rho}{dt} + \rho \nabla \cdot \mathbf{u} = 0, \qquad (11)$$

where $d/dt = \partial/\partial t + u\,\partial/\partial r$ denotes the convective derivative, and $\mathbf{u} = u\hat{r}$ is the velocity vector directed along the radial direction $\hat{r}$, and the conservation of energy, which we can write, dropping the viscous heating term, as

$$\rho C_p \frac{dT}{dt} + \frac{T}{\rho}\left(\frac{\partial\rho}{\partial T}\right)_p \frac{dp}{dt} = \nabla \cdot (K\nabla T). \qquad (12)$$

Here, T is the temperature, C_p is the specific heat at constant pressure, and K is the thermal conductivity of the gas. If the equation of continuity (11) is multiplied by $C_p T$ and added to (12), the result is

$$\frac{d}{dt}(C_p \rho T) + \frac{T}{\rho}\left(\frac{\partial\rho}{\partial T}\right)_p \frac{dp}{dt} + C_p \rho T \nabla \cdot \mathbf{u}$$

$$= \nabla \cdot (K\nabla T). \qquad (13)$$

We now assume that the gas can be adequately described by the perfect gas laws with constant specific heats. In this case, $C_p T\rho = \gamma p/(\gamma-1)$ and $(T/\rho)(\partial p/\partial T)_p = -1$. By (10), (13) can then be written as

$$\dot{p}/\gamma p + \nabla \cdot \{\mathbf{u} - [(\gamma-1)/\gamma p]K\nabla T\} = 0,$$

which, due to the spherical symmetry, can be integrated immediately to obtain the following expression for the velocity field:

$$u = \frac{1}{\gamma p}\left((\gamma-1)K\frac{\partial T}{\partial r} - \frac{1}{3}r\dot{p}\right). \qquad (14)$$

With the aid of the velocity boundary condition (3), this equation can be turned into a differential equation for p by evaluating it at $r = R$:

$$\dot{p} = \frac{3}{R}\left((\gamma-1)K\frac{\partial T}{\partial r}\bigg|_R - \gamma p\dot{R}\right). \qquad (15)$$

It may be noted that this equation may be equivalently written as

$$\frac{d}{dt}(pR^{3\gamma}) = 3(\gamma-1)R^{3\gamma-1}K\frac{\partial T}{\partial r}\bigg|_R,$$

from which one finds the adiabatic relation $pR^{3\gamma} = \text{const}$ when the heat loss through the bubble boundary is negligible. Under the same conditions, Eq. (14) shows the velocity distribution in the bubble to increase linearly with distance from the center.

In view of the approximation of uniform pressure, Eq. (14) and either one of the equations of continuity (11) or of energy (12) contain all the information present in the original set of equations. Since one can go from (11) to (12) by using (14) and the equation of state, the choice between the two is purely a matter of convenience. For this study, we choose to use the energy equation (12), which we rewrite explicitly as

$$\frac{\gamma}{\gamma-1}\frac{p}{T}\left(\frac{\partial T}{\partial t} + u\frac{\partial T}{\partial r}\right) - \dot{p} = \nabla \cdot (K\nabla T), \qquad (16)$$

with u given by (14). This choice was suggested by the fact that the thermal conductivity K will be allowed to depend on the temperature, as discussed below. Use of the continuity equation may also be considered in view of the fact that it would enable one to use conservative discretization of the spatial operators, although numerical stability may then become a concern.

At the bubble wall, the correct boundary conditions on the temperature field are continuity of temperature and heat fluxes. If D and D_L denote the thermal diffusivities in the gas and in the liquid, respectively, the temperature perturbations extend into the gas and the liquid for distances of the order of $(Dt_0)^{1/2}$ and $(D_L t_0)^{1/2}$ from the interface, where t_0 is the typical time already used. The heat flux from the gas to the interface can, therefore, be estimated to be of the order of $K(T_C - T_S)/(Dt_0)^{1/2}$, where T_C and T_S are the bubble center and surface temperatures, respectively. Similarly, the heat flux on the liquid side is $K_L(T_S - T_\infty)/(D_L t_0)^{1/2}$, where K_L is the liquid thermal conductivity and T_∞ is the undisturbed liquid temperature far from the bubble. Equating these two estimates of the heat fluxes, one finds

$$(T_S - T_\infty)/(T_C - T_S) \sim (KC_p \rho/K_L C_{pL}\rho_L)^{1/2}, \qquad (17)$$

where C_{pL} is the liquid specific heat. The ratio on the right-hand side has typical values in the range of 10^{-3}, which indicates that the surface temperature perturbation is but a small fraction of that of the gas and can, therefore, be neglected. In the preceding argument, we have implicitly assumed that $(Dt_0)^{1/2} < R$. In the opposite case, the gas in the bubble remains very nearly isothermal, and the preceding conclusion holds a fortiori. When the effect of the vapor is unimportant, we can, therefore, solve (16) subject to the condition

$$T(r = R, t) = T_\infty. \qquad (18)$$

This approximation simplifies the problem considerably since it asserts that a consideration of the temperature field in the liquid is unnecessary.

As the liquid temperature increases, the effect of evaporation and condensation renders (18) less and less accurate.

Suppose the bubble radius decreases by ΔR in a time t_0 and let ρ_V and L denote the vapor density and the latent heat, respectively. An amount of vapor of the order $\Delta m_V \sim 4\pi R^2 \Delta R \rho_V$ condenses with an amount of latent heat $L \Delta m_V$ available to increase the temperature of a liquid mass of the order of $4\pi R^2 (D_L t_0)^{1/2} \rho_L$. The predicted temperature rise $\Delta T \sim T_S - T_\infty$ is then

$$\frac{\Delta T}{T_\infty} \sim \frac{L}{C_{pL} T_\infty} \frac{\Delta R}{(D_L t_0)^{1/2}} \frac{\rho_V}{\rho_L}. \qquad (19)$$

For noncryogenic liquids, the first fraction in the right-hand side has typical values in the range 2–4. To estimate the second fraction, we consider resonance conditions and take $t_0 \sim 1/\omega_0$. Using (7), we then have

$$\frac{\Delta R}{(D_L t_0)^{1/2}} \sim \frac{\Delta R}{R} \left[\frac{R}{D_L} \left(\frac{p_\infty}{\rho_L} \right)^{1/2} \right]^{1/2}. \qquad (20)$$

For $R_0 = 0.1$ cm and $p_\infty = 1$ bar, the quantity in the square brackets is of the order of 100 and changes little with liquid properties, temperature, and pressure. The density ratio ρ_V/ρ_L, on the other hand, changes considerably with temperature. For water, for example, one has $\rho_V/\rho_L = 1.74\times10^{-5}, 8.44\times10^{-5}$, and 6.23×10^{-4} at $T = 20, 50$, and 100 °C, respectively. In this case, with the numerical values mentioned above, we find $\Delta T \sim 2.5\Delta R /R$ °C at 20 °C, but $\Delta T \sim 86\Delta R /R$ °C at 100 °C. These results actually overestimate the temperature increase since they presuppose that the condensation process is unhindered by the presence of the incondensible gas. In any case, they give a justification to the use of (18) even when vapor is present, provided the liquid is sufficiently cold.

During the motion of the bubble wall, the gas can undergo large variations in temperature, and the dependence of its thermal conductivity on this quantity cannot be neglected. A convenient way to account for this variation is to introduce the new variable

$$\tau = \int_{T_\infty}^{T} K(\theta) \, d\theta. \qquad (21)$$

Furthermore, for both analytical and numerical work, it is convenient to have a fixed rather than a moving boundary and we, therefore, let

$$y = r/R(t). \qquad (22)$$

With (14), (21), and (22), the energy equation (16) takes the form

$$\frac{\partial \tau}{\partial t} + \frac{\gamma - 1}{\gamma p R^2} \left(\frac{\partial \tau}{\partial y} - \frac{\partial \tau}{\partial y}\bigg|_{y=1} y \right) \frac{\partial \tau}{\partial y} - D\dot{p} = \frac{D}{R^2} \nabla^2 \tau, \qquad (23)$$

where the Laplacian is from now on with respect to the variable y, and

$$D(p,T) = \frac{K(T)}{C_p \rho(p,T)} = \frac{\gamma - 1}{\gamma} \frac{K(T)T}{p} \qquad (24)$$

is the appropriate form of the thermal diffusivity for a perfect gas. The boundary condition (18) is, in terms of τ,

$$\tau(y = 1, t) = 0. \qquad (25)$$

II. SUMMARY OF THE MATHEMATICAL FORMULATION AND NONDIMENSIONALIZATION

When the compressibility of the liquid is neglected, the motion of the bubble boundary is governed by the well-known Rayleigh–Plesset equation[7,25]

$$\rho_L (R\ddot{R} + \tfrac{3}{2}\dot{R}^2)$$
$$= p - p_\infty - p_S(t) - 2\sigma/R - 4\mu_L \dot{R}/R, \qquad (26)$$

where, as in Sec. I, p denotes the pressure in the bubble, p_∞ is the undisturbed liquid pressure, and $p_S(t)$ is a nonconstant ambient pressure component such as a sound field. The surface tension is denoted by σ and the liquid viscosity by μ_L. The effects of liquid compressibility can be approximately included using in place of (26) the equation of Keller and co-workers[11,13] or Herring[26] (see the discussion in Ref. 27). We have used the Keller formulation, given by

$$\left(1 - \frac{\dot{R}}{c} \right) R\ddot{R} + \frac{3}{2}\dot{R}^2 \left(1 - \frac{\dot{R}}{3c} \right)$$
$$= \left(1 + \frac{\dot{R}}{c} \right) \frac{1}{\rho_L} \left[p_B(t) - p_S\left(t + \frac{R}{c}\right) - p_\infty \right]$$
$$+ \frac{R}{\rho_L c} \frac{dp_B(t)}{dt}, \qquad (27a)$$

where c is the speed of sound in the liquid and $p_B(t)$ is the liquid pressure on the external side of the bubble wall, which is related to the internal bubble pressure $p(t)$ by

$$p(t) = p_B(R,t) + 2\sigma/R + 4\mu_L \dot{R}/R. \qquad (27b)$$

Equation (27) must be solved simultaneously with the energy equation in the bubble (23) and the equation for the internal pressure (15).

In the following, it will be convenient to make use of dimensionless quantities indicated temporarily by an asterisk. As a reference length, we use the equilibrium bubble radius

$$R_0 = 2\sigma/(p_0 - p_\infty), \qquad (28)$$

where p_0 is the internal pressure at equilibrium, which will be used as a reference pressure. As a reference time, we use the inverse of a typical frequency ω of the variable pressure field p_S. Therefore, we let

$$R = R_0 R_* , \quad t = t_*/\omega, \quad p = p_0 p_* , \quad p_\infty = p_0 p_{*\infty} ,$$
$$p_S = p_0 p_{*S} , \quad \tau = D_0 p_0 \tau_* , \quad T = T_\infty T_* , \qquad (29)$$
$$D = D_0 D_* ,$$

where

$$D_0 = \frac{K(T_\infty)}{C_p \rho(p_0, T_\infty)} = \frac{\gamma - 1}{\gamma} \frac{K(T_\infty)T_\infty}{p_0}$$

is the gas thermal diffusivity at equilibrium. In terms of these variables, Eqs. (27a), (23), and (15) governing the problem become, respectively,

$$\left(1 - \frac{U_*}{c_*} \right) R_* U_*' + \frac{3}{2}\left(1 - \frac{U_*}{3c_*} \right) U_*^2$$
$$= Z \left\{ \left(1 + \frac{U_*}{c_*} \right) \left[p_{B*} - p_{\infty *} - p_{S*}\left(t_* + \frac{R_*}{c_*} \right) \right. \right.$$
$$\left. \left. - \frac{W}{R_*} - M\frac{U_*}{R_*} \right] + \frac{R_*}{c_*} p_{B*}' \right\}, \qquad (30)$$

$$\frac{\partial \tau_*}{\partial t_*} + \frac{\gamma-1}{\gamma}\frac{\chi}{p_* R_*^2}\left(\frac{\partial \tau_*}{\partial y} - \frac{\partial \tau_*}{\partial y}\bigg|_{y=1} y\right)\frac{\partial \tau_*}{\partial y}$$

$$- D_* p'_* = \frac{\chi D_*}{R_*^2}\nabla^2 \tau_* \, , \tag{31}$$

$$p'_* = \frac{3}{R_*}\left((\gamma-1)\frac{\chi}{R_*}\frac{\partial \tau_*}{\partial y}\bigg|_{y=1} - \gamma p_* U_*\right), \tag{32}$$

where

$$U_* = R'_* \, ,$$

and the prime indicates differentiation with respect to the dimensionless time t_*. Furthermore, the following dimensionless parameters have been introduced:

$$\chi = D_0/\omega R_0^2 \, , \quad Z = p_0/\rho_L \omega^2 R_0^2 \, , \quad W = 2\sigma/R_0 p_0 \, ,$$
$$M = 4\mu_L \omega/p_0 \, , \quad c_* = c/\omega R_0 \, . \tag{33}$$

The dimensionless parameter χ is the square of the ratio of the thermal diffusion length to the bubble radius. Small values of χ correspond to a nearly adiabatic bubble, while large values of χ give rise to a nearly isothermal behavior of the gas. The following three dimensionless parameters represent ratios of pressure and inertia forces, surface tension and pressure, and viscous and pressure forces, respectively. It may be noted that it follows from (28) that

$$p_{*,\infty} = 1 - W \, .$$

In order to calculate D_*, it is necessary to find T_* by inverting the integral (21). For simplicity, in the calculations described in Sec. IV, we have approximated the dependence of K upon T by a linear function:

$$K = AT + B \, .$$

In this case, inversion of (21) leads to the following relation between T and τ:

$$T = \{[K^2(T_\infty) + 2A\tau]^{1/2} - B\}/A \tag{34a}$$

The numerical values $A = 5.28$ erg/cm s K^2, $B = 1165$ erg/cm s K give a good fit to the thermal conductivity of air in the range $200\,K < T < 3000\,K$. The dimensionless counterpart of (34a) is

$$T_* = (1/\alpha)\{\{1 + 2[(\gamma-1)/\gamma]\alpha\tau_*\}^{1/2} + \alpha - 1\}, \tag{34b}$$

where $\alpha = AT/K(T)$.

III. LINEAR OSCILLATIONS

As a first application of the previous model, we consider the case of small-amplitude oscillations. From now on, only nondimensional variables will be used and the asterisks will be dropped.

Upon linearization about the undisturbed state, Eqs. (31) and (32) become

$$\frac{\partial \tau}{\partial t} - p' = \chi \nabla^2 \tau \, , \tag{35}$$

$$p' = 3(\gamma-1)\chi\frac{\partial \tau}{\partial y}\bigg|_{y=1} - 3\gamma R' \, . \tag{36}$$

For a linear problem, one can consider each Fourier mode separately. Accordingly, since the frequency equals 1 in the

dimensionless units (29), we set

$$R = 1 + Xe^{it}, \quad p = 1 + Pe^{it}, \quad \tau = \Theta(y)e^{it}, \tag{37}$$

to find

$$\frac{\partial^2(y\Theta)}{\partial y^2} - \frac{i}{\chi}y\Theta = -\frac{i}{\chi}yP. \tag{38}$$

The solution finite at the origin and zero at $y = 1$ is

$$\Theta = P\left(1 - \frac{\sinh[(i/\chi)^{1/2}y]}{y\sinh(i/\chi)^{1/2}}\right). \tag{39}$$

Substitution of this result into (36) determines the pressure perturbation amplitude

$$P = -\Phi X, \tag{40}$$

with

$$\Phi = 3\gamma/\{1 - 3(\gamma-1)i\chi$$
$$\times [(i/\chi)^{1/2}\coth(i/\chi)^{1/2} - 1]\}. \tag{41}$$

This quantity is complex and, therefore, P may be thought of as consisting of a component in phase with X and one in phase with X':

$$P = -\text{Re}\,\Phi X - \text{Im}\,\Phi X' \, . \tag{42}$$

Upon substitution into the linearized form of the Rayleigh–Plesset equation,

$$X'' = Z(P - p_S + WX - MX') \, , \tag{43}$$

one finds

$$X'' = Z(M + \text{Im}\,\Phi)X' + Z(\text{Re}\,\Phi - W)X = -Zp_S \, , \tag{44}$$

i.e., an equation of the standard forced oscillator form with a damping constant $Z(M + \text{Im}\,\Phi)$ and a natural frequency $Z(\text{Re} - W)$. If the polytropic relation (1) were used, these quantities would have been found to be ZM and $Z(3\kappa - W)$, respectively. Thus a polytropic index can be defined by

$$\kappa = \tfrac{1}{3}\text{Re}\,\Phi \, , \tag{45}$$

but no real value of κ would result in the correct amount of damping. To remedy this situation, it was suggested in Ref. 12 to define an effective viscosity parameter M_e such that

$$M_e = M + \text{Im}\,\Phi \, , \tag{46}$$

i.e., compare with (33),

$$\mu_{L,e} = \mu_L + (p_0/4\omega)\text{Im}\,\Phi \, , \tag{47}$$

which then was to be used in the Rayleigh–Plesset equation. The preceding results show that this suggestion is justified for linear oscillations, but it will be shown in later sections that the nonlinear regime may behave quite differently. For a more complete discussion of these linear results and graphs of κ and $\text{Im}\,\Phi$, the reader is referred to Ref. 28. Here, we note that the dimensional results for the resonance frequency ω_0 and the total damping coefficient β are

$$\omega_0^2 = (p_0/\rho R_0^2)(\text{Re}\,\Phi - 2\sigma/R_0 p_0) \, ,$$

$$2\beta = 4\mu_L/\rho R_0^2 + (p_0/\rho_L \omega R_0^2)\text{Im}\,\Phi \, .$$

It can readily be verified that (39) and (41) coincide with the expressions obtained by Pfriem[1] and rederived by Devin.[2] However, an essential aspect of the bubble behavior, which perhaps has not been adequately stressed by these

authors, is that, unlike the case of a standard mechanical oscillator, the effective damping and resonance frequency depend on the frequency of the driving signal, as is clear from (41) and the definition (33) of χ. A gas bubble responds as a linear oscillator only when driven at a single frequency. Its response under multiple-frequency or nonperiodic excitation is far more complex and depends also on the past history of the motion.[29]

IV. NUMERICAL RESULTS

We proceed now to discuss some numerical results for large-amplitude oscillations with our new formulation and to compare them with the predictions based upon the polytropic approximation. These results are far from exhaustive and are presented here primarily to demonstrate the usefulness and range of applicability of the present formulation. In the calculations, we have used the following values of the physical parameters: $p_\infty = 1$ bar, $T_\infty = 20$ °C, $\gamma = 1.4$, $\rho_L = 1$ g/cm^3, $\mu_L = 1$ cP, $\sigma = 72.8$ erg/cm^2, $c = 1481$ m/s.

For all the examples to be considered, the driving sound field p_S appearing in (27a) is given, in dimensional form, by $p_S = -\epsilon p_\infty \sin \omega t$ and, in dimensionless form, by

$$p_{S*} = -\epsilon(1 - W)\sin t_* .\qquad (48)$$

Here, ϵ is the dimensionless sound amplitude.

In the following, when we refer to the *present model*, we indicate our new formulation of bubble dynamics in which the internal pressure is calculated directly and the Keller radial equation of motion (27) is used. The words *polytropic model*, on the other hand, will indicate use of the Keller equation with a polytropic relation for the internal pressure corrected by the addition of a fictitious "thermal viscosity" term, as was mentioned in the Introduction and in Sec. III. Specifically, we take

$$p_{\text{pol}} = p_0(R_0/R)^{3\kappa(\omega)} - 4\mu_{\text{th}} \dot{R}/R ,\qquad (49)$$

where from (47),

$$\mu_{\text{th}} = (p_0/4\omega_0)\text{Im}\,\Phi(\omega_0) .\qquad (50)$$

In (49), the polytropic index is evaluated at the driving frequency ω. This is necessary to ensure the appropriate "stiffness" of the bubble, but such an unambiguous selection is only possible when the driving sound field is monochromatic, as in the present examples. The thermal viscosity, on the other hand, is evaluated at the linear resonance frequency ω_0. The rationale for this procedure was given in Ref. 14 and is as follows. Both in the case of nonsinusoidal and nonlinear oscillations, the bubble motion can be seen as consisting of

the superposition of a number of oscillators at different frequencies. If only one frequency can be selected for the damping, this should be chosen to be close to the mode that is most affected by energy dissipation, i.e., the resonant mode. Since the damping is relatively small, all other modes will be affected only slightly anyway. Experimental results indicate that this procedure, although far from being exact, improves agreement with data.[14] For the same reason, one may define an effective "acoustic viscosity" for use with the Rayleigh–Plesset equation (26) by

$$\mu_{\text{ac}}(\omega_0) = \rho_L R_0^3 \omega_0^2/4c .$$

Equation (49) may be regarded as a parametrization of the thermal energy dissipation patterned after the viscous one. The inverse proportionality to the radius gives a larger effect near radius minima, where the bubble has a higher temperature and a smaller size, and this feature appears, at least qualitatively, correct. On the other hand, as will be seen in the following numerical examples, during much of the oscillation, the radius is relatively large and the velocity relatively small, so that little thermal energy would be dissipated according to (49) in these portions of the cycle. One may say that (49) concentrates energy dissipation in "bursts" around the radius minima. The net result over one cycle of steady oscillation can, depending on circumstances, be bigger or smaller than that predicted by the present model as can be seen in Table I. Here, in addition to the maximum and minimum dimensionless radii during a cycle of steady oscillation, we show the dimensionless average power dissipated per cycle and defined by

$$\mathscr{P}_* = \mathscr{P}/4\pi R_0^3 \omega p_\infty \epsilon^2 ,\qquad (51)$$

with the dimensional average power $\mathscr{P}$ calculated from

$$\mathscr{P} = \frac{\omega}{2\pi} \int_0^{2\pi/\omega} 4\pi R^2 \dot{R} p_S(t)\, dt .\qquad (52)$$

Note that, with the nondimensionalization (51), the linear value of $\mathscr{P}_*$ is independent of the driving pressure amplitude ϵ.

We begin by showing in Figs. 1 and 2 a comparison between the frequency response curves calculated with the present theory and the polytropic formulation for a sound-pressure amplitude $\epsilon = 0.6$ and equilibrium bubble radii of 50 and 10 μm, respectively. These graphs display for each value f/f_0 of the ratio of the sound frequency to the resonance frequency (calculated from linear theory) the maximum of the oscillation amplitude defined by

$$X = (R_{\text{max}} - R_0)/R_0 ,\qquad (53)$$

TABLE I. Computed values of the dimensionless average power dissipation and maximum and minimum radius for the cases illustrated in the figures.

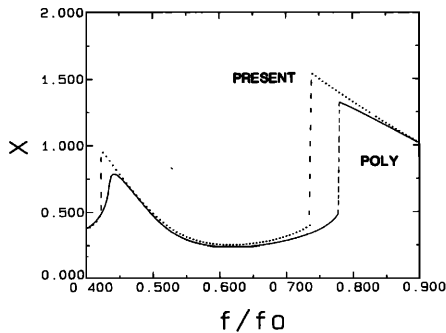| $R_0(\mu m)$	f/f_0	$\mathscr{P}_*$		$R_{*\text{max}}$		$R_{*\text{min}}$	
		Present	Polytropic	Present	Polytropic	Present	Polytropic
50	0.8	0.69	1.1	2.33	2.27	0.327	0.209
50	0.6	0.56	0.49	1.26	1.24	0.663	0.645
50	0.44	0.45	0.46	1.84	1.78	0.402	0.339
10	0.8	1.2	0.25	2.39	1.54	0.244	0.425
10	0.44	0.16	0.22	1.49	1.55	0.595	0.503

FIG. 1. Frequency response curves for the forced oscillations of a bubble of radius 50 μm in water at 20 °C for a dimensionless acoustic amplitude ϵ = 0.6. The two curves show the results predicted by the polytropic model and the present formulation in which the internal pressure is evaluated directly; X is the normalized amplitude of the radial oscillations defined in Eq. (53). The horizontal scale is the frequency of the driving sound made dimensionless by the linear resonance frequency defined in Sec. III.

where R_{max} is the maximum value attained by the radius during a steady oscillation. Similar curves have been obtained by several other investigators[9,30–32] to explore the nonlinear characteristics of bubble oscillations. The solid line is the polytropic model, and the dotted line denotes results obtained from the present model. The most striking difference between the two formulations consists in the location and the height of the peaks corresponding to the fundamental and the higher resonances. The relative shift between these peaks in some cases results in considerable differences between the two oscillation amplitudes at a given frequency. Also, the positions at which the response exhibits a large jump are very strongly affected. These structures are well known in nonlinear oscillations and, in the context of bubble dynamics, have been studied in Ref. 12. The transition to subharmonic oscillations and chaotic motion is determined by similar jumps which appear at larger driving amplitudes in other frequency regions. It may, therefore, be expected that these transitions will likewise appear different in the two models.
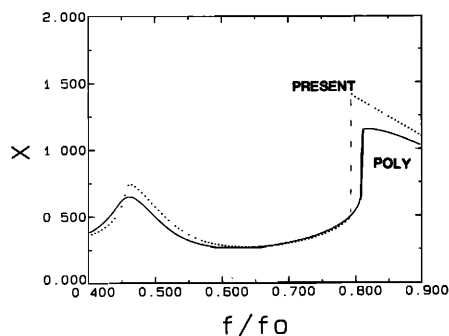
We now turn to a detailed examination of the oscillations at two different values of f/f_0. The first value is 0.8, and can be seen from Figs. 1 and 2 to be on the main resonance peak. The second one is 0.44 and lies on the second harmonic peak. For the case of the larger bubble, we also consider $f/f_0 = 0.6$, at which the two models are seen in Fig. 1 to closely agree.

Figure 3 shows a comparison of the $R(t)$ curves according to the present theory and to the polytropic formulation for $R_0 = 50$ μm. The present model predicts a larger maximum radius, but the polytropic one results in a minimum radius which is about 50% smaller (see Table I). The pressure history, shown in Fig. 4(a) and (b) to linear and logarithmic scales, respectively, is correspondingly much more peaked for the polytropic case. As shown in Table I, the polytropic model overestimates by nearly 50% the absorbed power. Although rather speculative, the following considerations based on the comments made earlier on Eq. (49) may explain these results. Since little energy is dissipated by the polytropic model during the relatively long fraction of the cycle where the bubble has a large radius, the collapse point is approached with a large velocity, and the minimum radius is correspondingly smaller. In turn, the large velocity and small radius give rise to an excessive energy dissipation presumably concentrated in a large burst near the point of minimum radius.

The ratio $\chi^{1/2}$ of the thermal diffusion length to the bubble radius [cf. Eq. (33)] is, in this case, 0.169, which implies that the thermal wave does not penetrate too deeply into the bubble, as will be discussed below. If the value of f/f_0 is kept fixed and the radius is increased, χ decreases and the process becomes more and more adiabatic. For this reason, the behavior of bigger bubbles can be expected not to deviate very much from the 50-μm case illustrated here.

The situation is markedly different in the case of the smaller bubble, $R_0 = 10$ μm, the behavior of which at $f/f_0 = 0.8$ and $\epsilon = 0.6$ is illustrated in Figs. 5 and 6. Now the $R(t)$ curves, computed according to the present theory and the polytropic formulation, are remarkably dissimilar with a large phase shift and a significant difference in the oscillation
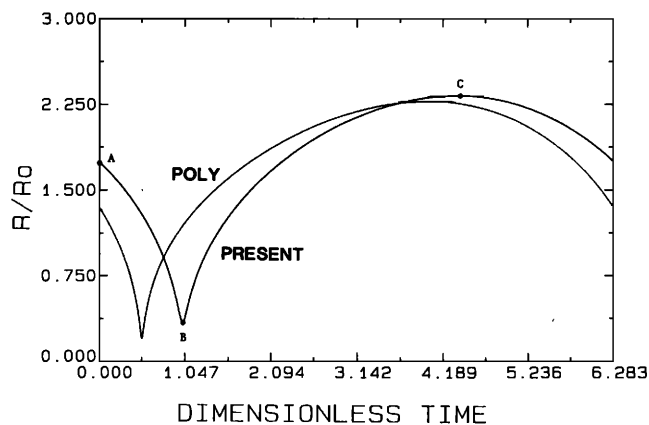

FIG. 2. Frequency-response curves for the forced oscillations of a bubble of radius 10 μm in water at 20 °C for a dimensionless acoustic amplitude ϵ = 0.6. The two curves show the results predicted by the polytropic model and the present formulation in which the internal pressure is evaluated directly; X is the normalized amplitude of the radial oscillations defined in Eq. (53). The horizontal scale is the frequency of the driving sound made dimensionless by the linear resonance frequency defined in Sec. III.

FIG. 3. Normalized radius–time curves for the steady oscillations of a 50-μm bubble driven at a dimensionless acoustic pressure amplitude $\epsilon = 0.6$ and a frequency ratio of 0.8. The two curves show the results predicted by the present formulation and the polytropic model.
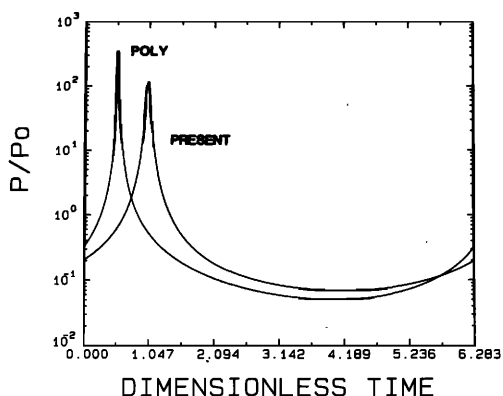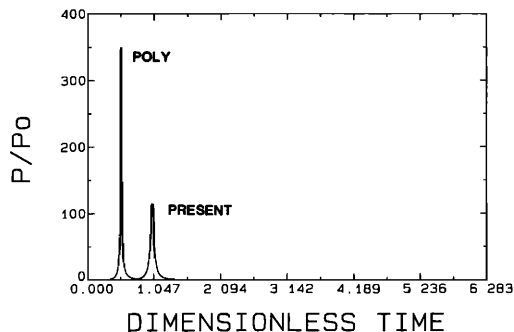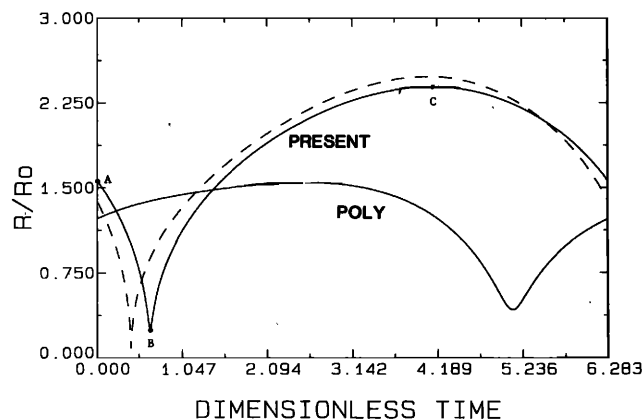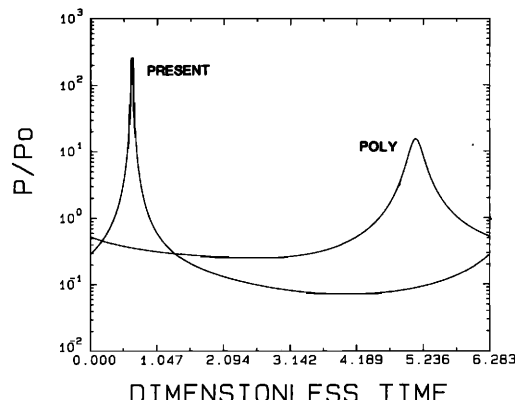
FIG. 4. Normalized pressure–time histories for the steady oscillations of a 50-μm bubble shown in Fig. 3. The two curves show the results predicted by the two models. In (a) the ordinate, plotted to a linear scale, shows the large difference between the maximum values of the pressure. In (b) the ordinate, plotted to a log scale, shows that the two curves are significantly different throughout the cycle. The dimensionless acoustic pressure amplitude is $\epsilon = 0.6$, and the frequency ratio is 0.8.

FIG. 6. Normalized pressure–time histories for the steady oscillations of a 10-μm bubble shown in Fig. 5. The two curves show the results predicted by the two models. In (a) the ordinate is plotted to a linear scale and in (b) to a log scale. The dimensionless acoustic pressure amplitude is $\epsilon = 0.6$, and the frequency ratio 0.8.

amplitudes. According to Table I, energy dissipation is underpredicted by a factor of nearly 5 by the polytropic model. A comparison of the two curves shows that this is not due to a smaller overall damping coefficient, but to smaller oscillation amplitude and velocity, much in the same way as for a

FIG. 5. Normalized radius–time curves for the steady oscillations of a 10-μm bubble driven at a dimensionless acoustic pressure amplitude $\epsilon = 0.6$ and a frequency ratio of 0.8. The two curves show the results predicted by the present formulation and the polytropic model. The dashed line is the polytropic result for a dimensionless pressure amplitude $\epsilon = 1$.
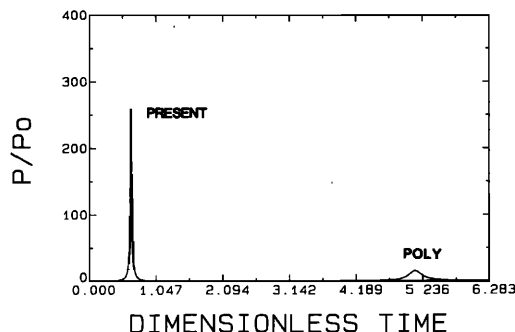
heavily damped linear oscillator. In the framework of Eq. (49), it appears that the radius does not grow enough to effectively "switch off" the energy dissipation term. That this is the correct explanation is suggested by the fact that, raising the driving amplitude to $\epsilon = 1$ (dashed line), a pattern much more similar to that of Fig. 3 emerges. The internal pressure for this case with $\epsilon = 0.6$ is shown in Fig. 6. Due to the reduced amplitude of oscillation, it is the polytropic peak that is lower and, because of the phase difference, shifted with respect to the position obtained with the exact theory.

We consider next the results in the region of the second harmonic resonance, $f/f_0 = 0.44$. Figure 7 refers to $R_0 = 50$ μm again for $\epsilon = 0.6$. The two minima around $t_* = 4$, which may essentially be attributed to the Fourier component at ω, are comparable to each other in a manner similar to that of Fig. 3. The second-harmonic components at 2ω, on the other hand, appear to be out of phase, not unlike the situation found in Fig. 5. Again, this may be attributed to the larger damping of the polytropic model which affects more strongly the smaller harmonic component. The pressure–time history for this case, shown in Fig. 8, can likewise be interepreted as a combination of Figs. 4 and 6 for the two components.

The behavior of the smaller bubble, $R_0 = 10\,\mu$m, in the region of the second harmonic is shown in Figs. 9 and 10. Due to the effect of surface tension, as can be seen from Eq.
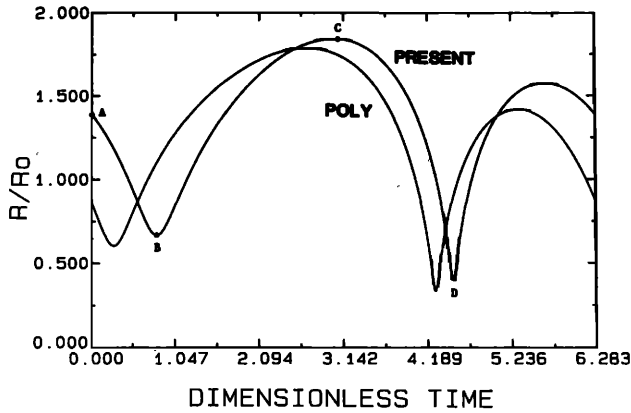
FIG. 7. Normalized radius–time curves for the steady oscillations of a 50-μm bubble driven at a dimensionless acoustic pressure amplitude $\epsilon = 0.6$ and a frequency ratio 0.44. The two curves show the results predicted by the present formulation and the polytropic model.

FIG. 9. Normalized radius–time curves for the steady oscillations of a 10-μm bubble driven at a dimensionless acoustic pressure amplitude $\epsilon = 0.6$ and a frequency ratio of 0.44. The two curves show the results predicted by the present formulation and the polytropic model.

(48), bubbles become stiffer as the radius is decreased, and, therefore, the oscillation amplitude is smaller than for $R_0 = 50$ μm. This has the effect that differences are not as evident in the radius–time curves (Fig. 9), although they are clearly demonstrated in the pressure–time curves of Fig. 10.

As a last example, we have considered $f/f_0 = 0.6$ for $R_0 = 50$ μm and $\epsilon = 0.6$. It can be seen from Fig. 1 that for this value of the frequency, the oscillation amplitudes are relatively small and quite close. Therefore, not much difference between the two models is expected, in agreement with the results of Table I. The radius–time curves for this case are shown in Fig. 11, where they can barely be distinguished.

The question of under what circumstances is the polytropic model acceptable is not easy to answer. Clearly, the criterion cannot be solely based on the oscillation amplitude as computed from the polytropic model itself. The good agreement of Fig. 11 is found because the oscillation amplitude is relatively small, but also, very importantly, because the bubble is driven far from resonances. The amplitude in Fig. 9 is comparable to that in Fig. 5, but, in the first case, the comparison is good, while, in the second one, it is very bad. The key here is the difference between the resonance structures of Fig. 2. It might then be suggested that, away from
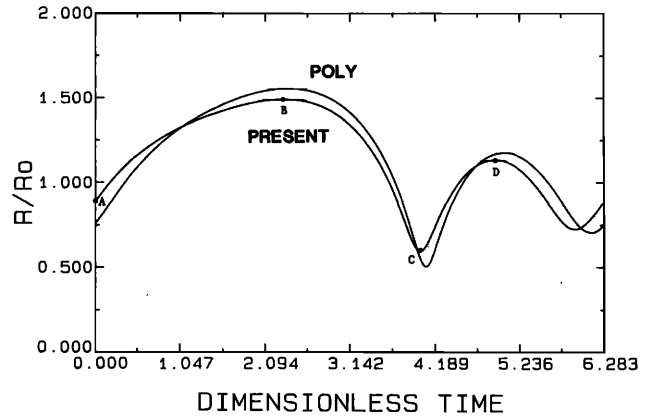
frequencies corresponding to resonances, the comparison should be good provided the amplitude is not too large (say, $X \lesssim 0.7$ as indicated by Figs. 7 and 9). Even this criterion must be used very cautiously, however, since, with increased driving, the resonant peaks broaden and new resonances appear.[9] In the light of these considerations, the polytropic model appears to be unreliable, not because it consistently leads to bad results, but rather because it is hard to decide a priori whether it is adequate for a given application.

Finally, we show in Figs. 12 to 15 some temperature profiles in the bubbles at different times during the oscillation. The instants of time at which these profiles are taken are marked on the corresponding radius–time curves in Figs. 3, 5, 7, and 9. Figure 12 refers to the 50-μm bubble at $f/f_0 = 0.8$. As already remarked, the value of χ is small in this case, $\chi = 0.0286$, and the gas is, to some extent, shielded from the liquid with a resulting nearly adiabatic behavior over a good part of the bubble interior. The maximum temperature, reached at the point of minimum radius, is close to 3000 K which is more than sufficient for the production of free radicals and sonoluminescent effects. The other temperature profiles in this figure are taken at the beginning of the cycle and at the point of maximum radius. The tempera-
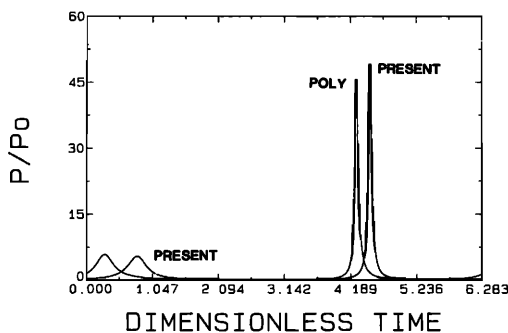

FIG. 8. Normalized pressure–time histories for the steady oscillations of a 50-μm bubble shown in Fig. 7. The two curves show the results predicted by the two models. The dimensionless acoustic pressure amplitude is $\epsilon = 0.6$, and the frequency ratio 0.44.
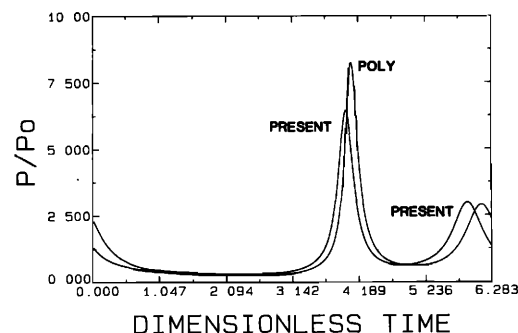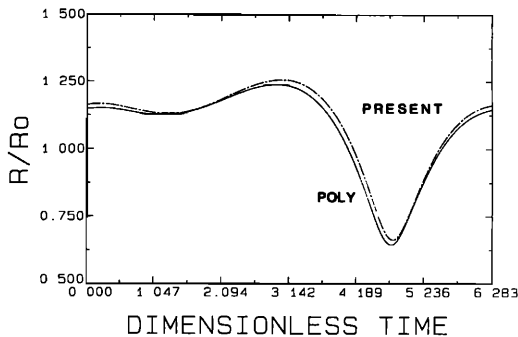

FIG. 10. Normalized pressure–time histories for the steady oscillations of a 10-μm bubble shown in Fig. 9. The two curves show the results predicted by the two models. The dimensionless acoustic pressure amplitude is $\epsilon = 0.6$, and the frequency ratio 0.44.

FIG. 11. Normalized radius–time curves for the steady oscillations of a 50-μm bubble driven at a dimensionless acoustic pressure amplitude $\epsilon = 0.6$ and a frequency ratio of 0.6. The dashed line shows the result predicted by the present formulation, and the solid line that of the polytropic model.

FIG. 13. Temperature distributions in the interior of a 10-μm bubble in steady oscillation with $\epsilon = 0.6$, $f/f_0 = 0.8$ at different instants of time. The conditions are the same as in Fig. 5. The letters refer to the points indicated in Fig. 5 and mark the time at which each distribution is shown.

ture effect is obviously much less spectacular during the cooling portions since the dimensionless temperature can only range between 1 (i.e., the undisturbed value) and 0. It is interesting to note that the minimum center temperature is not reached exactly at the point of maximum radius but a little earlier due to the heat received from the liquid. Figure 13 refers to the case at $f/f_0 = 0.44$ of Fig 7. The value of χ is now somewhat larger, $\chi = 0.0521$ ($\chi^{1/2} = 0.228$), and the bubble interior is, therefore, more affected by the presence of the liquid. These changes in the temperature distribution lie at the basis of the dependence of the thermal damping and polytropic exponent with the driving frequency, to which attention was called in Refs. 3 and 28 on the basis of the linear theory.

Figures 14 and 15 are for the 10-μm bubble at $f/f_0 = 0.8$ and 0.44 and for values of $\chi = 0.132$ ($\chi^{1/2} = 0.364$) and $\chi = 0.241$ ($\chi^{1/2} = 0.491$), respectively. No new features emerge here except for the curve labeled A in Fig. 15, which shows the occurrence of a nonmonotonic temperature profile.
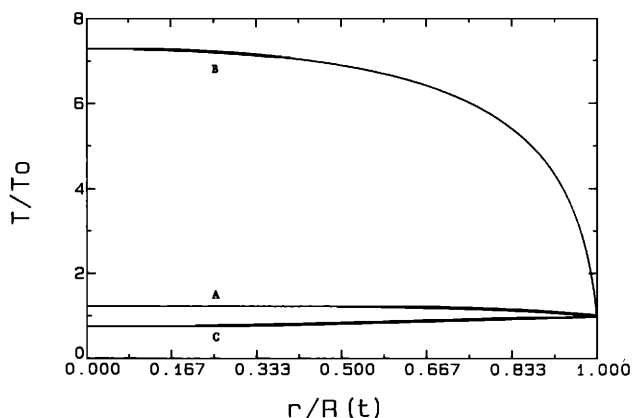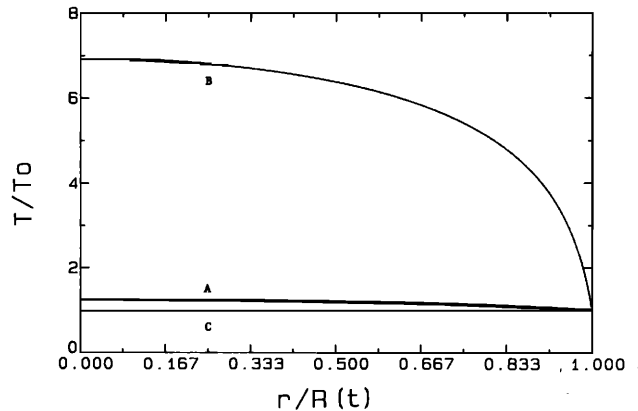
V. SUMMARY AND CONCLUSIONS

It has been shown that a new formulation of bubble dynamics based upon a direct evaluation of the internal pressure within the bubble can give considerably different predictions of behavior when compared with the standard treatment in which the internal pressure is approximated by a polytropic relation and use is made of an effective viscosity. The radius–time curves predicted by the two models can differ very markedly (see, for example, Fig. 5), and the calculated values of energy dissipation in a cycle do not reveal a systematic pattern in their discrepancies (see Table I). The differences are especially large in the frequency regions corresponding to linear and nonlinear resonances.

A general conclusion that may be drawn from the above comparison is that the polytropic model is unreliable in accounting for the dissipation of energy by thermal processes, especially at large pulsation amplitudes. Therefore, it may result in very poor predictions of the bubble behavior whenever these processes are the dominant form of energy dissipation.
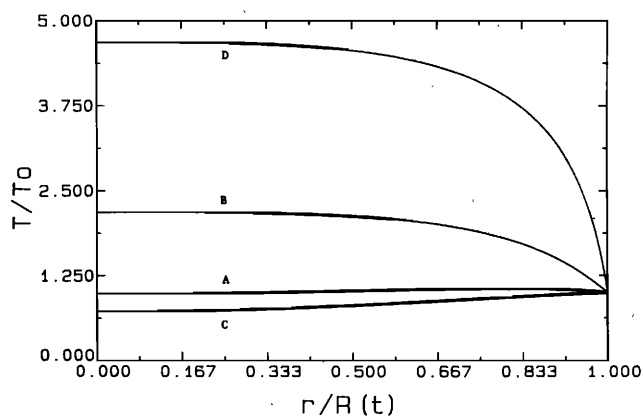

FIG. 12. Temperature distributions in the interior of a 50-μm bubble in steady oscillation with $\epsilon = 0.6$, $f/f_0 = 0.8$ at different instants of time. The conditions are the same as in Fig. 3. The letters refer to the points indicated in Fig. 3 and mark the time at which each distribution is shown.

FIG. 14. Temperature distributions in the interior of a 50-μm bubble in steady oscillation with $\epsilon = 0.6$, $f/f_0 = 0.44$ at different instants of time. The conditions are the same as in Fig. 7. The letters refer to the points indicated in Fig. 7 and mark the time at which each distribution is shown.
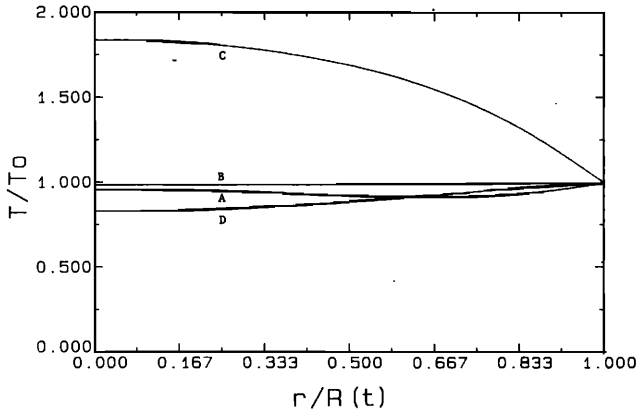
FIG. 15. Temperature distributions in the interior of a 10-μm bubble in steady oscillation with $\epsilon = 0.6$, $f/f_0 = 0.44$ at different instants of time. The conditions are the same as in Fig. 9. The letters refer to the points indicated in Fig. 9 and mark the time at which each distribution is shown.

ACKNOWLEDGMENTS

APPENDIX: OUTLINE OF THE NUMERICAL METHOD

All the quantities appearing in this Appendix are dimensionless, but the asterisks have been dropped.

The system to be solved consists of the radial equation (30), the pressure equation (32), and temperature equation (31). The first two are ordinary differential equations, while the last one is a partial differential equation. We begin by carrying out a spatial discretization on this last equation by introducing $N + 1$ equispaced points $y_k = (k - 1)\Delta y$, $k = 1,2,...,N + 1$, with $y_1 = 0$, $y_{N+1} = 1$, and $\Delta y = 1/N$. On this grid we use the following approximations for the spatial differential operators:

$$(\nabla^2 \tau)_i \cong \frac{1}{\Delta y^2}\left[\left(1 + \frac{\Delta y}{y_i}\right)\tau_{i+1}\right.$$
$$\left. - 2\tau_i + \left(1 - \frac{\Delta y}{y_i}\right)\tau_{i-1}\right],$$ (A1)

$$\left(\frac{\partial \tau}{\partial y}\right)_i \cong \frac{\tau_{i+1} - \tau_{i-1}}{2\Delta y},$$ (A2)

where the index i indicates evaluation at the node y_i. These two expressions are used for all internal nodes. For the first node, the appropriate expressions are

$$(\nabla^2 \tau)_1 \cong 6(\tau_2 - \tau_1)/\Delta y^2,$$ (A3)

$$\left(\frac{\partial \tau}{\partial y}\right)_1 = 0,$$ (A4)

while at the bubble wall

$$\left(\frac{\partial \tau}{\partial y}\right)_{N+1} \cong \frac{3\tau_{N+1} - 4\tau_N + \tau_{N-1}}{2\Delta y} = \frac{\tau_{N-1} - 4\tau_N}{2\Delta y},$$ (A5)

since $\tau_{N+1} = 0$ according to (25). With these definitions, we can rewrite the temperature equation (31) in the discretized form:

$$\frac{\partial \tau_i}{\partial t} \equiv \tau_i' = D_i\left(\frac{\chi}{R^2}(\nabla^2 \tau)_i + p'\right)$$
$$+ \frac{\gamma - 1}{\gamma}\frac{\chi}{pR^2}\left[\left(\frac{\partial \tau}{\partial y}\right)_{N+1} y_i - \left(\frac{\partial \tau}{\partial y}\right)_i\right]\left(\frac{\partial \tau}{\partial y}\right)_i,$$ (A6)

where $i = 1,2,..., N$, and $D_i = D(\tau_i)$. We shall first give an overview of the numerical method and then furnish the pertinent details.

Equations (A6) can be considered as a set of ordinary differential equations in the unknowns $\tau_1,\tau_2,...,\tau_N = \{\tau_i\}$. If R, U, p, and all the τ_i's are arranged into a single vector of unknowns $\mathbf{X}$, schematically one can write the system (30) (32), and (A6) in the form

$$\frac{d\mathbf{X}}{dt} = \mathbf{F}(\mathbf{X},t).$$ (A7)

The vector function $\mathbf{F}$ is shorthand for the right-hand sides of the equations, and its explicit dependence on time occurs only due to the forcing pressure term p_S in the radial equation (30). An approximate solution to (A7) can be written using the trapezoidal rule as

$$\mathbf{X}^{n+1} = \mathbf{X}^n + (\Delta t/2)[\mathbf{F}(\mathbf{X}^n,t^n) + \mathbf{F}(\mathbf{X}^{n+1},t^{n+1})],$$

or, with an obvious notation,

$$\mathbf{X}^{n+1} = \mathbf{X}^{n+1/2} + (\Delta t/2)\mathbf{F}(\mathbf{X}^{n+1},t^{n+1}).$$ (A8)

Here, Δt is the time step and superscripts indicate time levels. Equation (A8) is highly implicit due to the appearance of the advanced-time solution $\mathbf{X}^{n+1}$ both in the left-hand side and in the complicated nonlinear function $\mathbf{F}$ in the right-hand side. This equation is, therefore, difficult to solve as it stands. However, since it approximates (A7) with an error term of order Δt^3, we only need to solve it with an $O(\Delta t^3)$ accuracy for the whole procedure to be consistent. This goal can be obtained as follows. Start by generating a low-accuracy approximation $\tilde{\mathbf{X}}$ to $\mathbf{X}^{n+1}$ by using a simple Euler explicit integration,

$$\tilde{\mathbf{X}} = \mathbf{X}^n + \mathbf{F}(\mathbf{X}^n,t^n)\Delta t.$$ (A9)

This can now be used in the right-hand side of (A8) to obtain an improved estimate $\bar{\mathbf{X}}$ of $\mathbf{X}^{n+1}$,

$$\bar{\mathbf{X}} = \mathbf{X}^{n+1/2} + \tfrac{1}{2}\Delta t\,\mathbf{F}(\tilde{\mathbf{X}},t^{n+1}).$$ (A10)

Since the error in (A9) is of order Δt^2, (A10) already has a formal error of order Δt^3 and, hence, one could set $\mathbf{X}^{n+1} = \bar{\mathbf{X}}$. However, it is better to apply the same procedure once more to finally obtain

$$\mathbf{X}^{n+1} = \mathbf{X}^{n+1/2} + \tfrac{1}{2}\Delta t + \mathbf{F}(\bar{\mathbf{X}},t^{n+1}).$$ (A11)

In the concrete application of this method, which will now be described, we exploit the specific form of $\mathbf{F}$ to retain some of the implicitness present in (A8) for greater stability.

Suppose the solution has been completely determined up to time t^n. Then we begin by generating the first Euler estimate (A9) by

$$\tilde{\tau}_i = \tau_i^n + \Delta t\tau_i'^n, \quad 1 \leq i \leq N,$$ (A12a)

$$\tilde{U} = U^n + \Delta t U'^n, \tag{A12b}$$

$$\tilde{p} = p^n + \Delta t p'^n, \tag{A12c}$$

$$\tilde{R} = R^n + \Delta t U^n, \tag{A12d}$$

with $\tau_i'^n$ given by (A6) U'^n by (30), and p'^n by (32), all evaluated in terms of the known values at t^n. In particular,

$$p'^n = \frac{3}{R^n}\left(\frac{(\gamma-1)}{2R^n\Delta y}(\tau_{N-1}^n - 4\tau_N^n) - \gamma p^n U^n\right). \tag{A13}$$

The values (A12a) are used to compute the thermal diffusivity according to the dimensionless analog of (24); i.e.,

$$D = (\alpha T + 1 - \alpha) T/p,$$

with T calculated from (34b).

At the next step, we execute (A10) introducing, as anticipated, some slight modifications for greater stability. For the temperature equation, we write

$$\overline{\tau}_i = \tau_i^{n+1/2} + \frac{1}{2}\Delta t\left[\tilde{D}_i\left(\frac{\chi}{\tilde{R}^2}(\nabla^2\overline{\tau})_i + \tilde{p}'\right)\right.$$
$$\left. + \frac{\gamma-1}{\gamma}\frac{\chi}{\tilde{p}\tilde{R}^2}\left[\left(\frac{\partial\overline{\tau}}{\partial y}\right)_{N+1}y_i - \left(\frac{\partial\overline{\tau}}{\partial y}\right)_i\right]\left(\frac{\partial\overline{\tau}}{\partial y}\right)_i\right]. \tag{A14}$$

Note that the barred values appear also in the right-hand side, so that this equation is not explicit in $\{\overline{\tau}_i\}$. However, if all the space operators are written out in full, it is realized that the N equations (A14) form a linear tridiagonal system, which can very readily be solved by well-known methods. The generic equation of this system has the form

$$A_i\overline{\tau}_{i-1} + B_i\overline{\tau}_i + C_i\overline{\tau}_{i+1} = F_i, \tag{A15}$$

where

$$A_i = \frac{\Delta t\chi}{2\tilde{R}^2\Delta y^2}\left\{-\tilde{D}_i\left(1 - \frac{\Delta y}{y_i}\right)\right.$$
$$\left. + \frac{\gamma-1}{\gamma}\frac{\Delta y}{\tilde{p}}\left[\left(\frac{\partial\overline{\tau}}{\partial y}\right)_{N+1}y_i - \left(\frac{\partial\overline{\tau}}{\partial y}\right)_i\right]\right\}, \tag{A16a}$$

$$B_i = 1 + \Delta t\chi\tilde{D}_i/\tilde{R}^2\Delta y^2, \tag{A16b}$$

$$C_i = -\frac{\Delta t\chi}{2\tilde{R}^2\Delta y^2}\left\{\tilde{D}_i\left(1 + \frac{\Delta y}{y_i}\right)\right.$$
$$\left. + \frac{\gamma-1}{\gamma}\frac{\Delta y}{\tilde{p}}\left[\left(\frac{\partial\overline{\tau}}{\partial y}\right)_{N+1}y_i - \left(\frac{\partial\overline{\tau}}{\partial y}\right)_i\right]\right\}, \tag{A16c}$$

$$F_i = \tau_i^{n+1/2} + \frac{1}{2}\Delta t\tilde{D}_i\tilde{p}'. \tag{A16d}$$

These expressions apply for $2\leqslant i\leqslant N$ except that, for $i = N$, the last term in the left-hand side of (A15) vanishes since $\tau_{N+1} = 0$. At the first spatial node, $i = 1$, the coefficients take a somewhat different form due to (A3) and (A4). Specifically, one has

$$A_1 = 0, \tag{A17a}$$

$$B_1 = 1 + 3\Delta t\chi\tilde{D}_1/\Delta y^2\tilde{R}^2, \tag{A17b}$$

$$C_1 = -3\Delta t\chi\tilde{D}_1/\Delta y^2\tilde{R}^2, \tag{A17c}$$

$$F_1 = \tau_1^{n+1/2} + (\Delta t/2)\tilde{D}_1\tilde{p}'. \tag{A17d}$$

Once the system (A15) has been solved, the temperatures $\{\overline{T}\}_i$ are computed using (34b) after which the $\overline{D}_i$'s can be obtained as before.

A similar degree of implicitness is used in the other equations. For the radial velocity, we write

$$\overline{U} = U^{n+1/2} + \frac{\Delta t}{2\tilde{R}[1 - (\tilde{U} + ZM/\tilde{R})/c_*]}$$
$$\times\left\{-\frac{3}{2}\left(1 - \frac{\tilde{U} + 8ZM/\tilde{R}}{3c_*}\right)\tilde{U}\,\overline{U}\right.$$
$$+ Z\left(1 + \frac{\tilde{U}}{c_*}\right)\left[\tilde{p} - p_\infty - p_S\left(t^{n+1} + \frac{\tilde{R}}{c_*}\right)\right.$$
$$\left. - \frac{W + M\tilde{U}}{\tilde{R}}\right] + Z\frac{\tilde{R}}{c_*}\tilde{p}'\right\}, \tag{A18}$$

where Z, W, M, and c_* are given in (33). This form is obtained by writing $U^2 \cong \tilde{U}\,\overline{U}$ and by using $\overline{U}$ rather than $\tilde{U}$ in the viscous term. The new value of the radius is computed from

$$\overline{R} = R^{n+1/2} + \frac{1}{2}\Delta t\overline{U}, \tag{A19}$$

while, for the pressure, we write

$$\overline{p} = p^{n+1/2} + \frac{3\Delta t}{2\overline{R}}\left[\frac{(\gamma-1)\chi}{\overline{R}}\left(\frac{\partial\overline{\tau}}{\partial y}\right)_{N+1} - \gamma\overline{p}\,\overline{U}\right], \tag{A20}$$

which is again implicit in $\overline{p}$.

The last step (A11) is identical to the one just executed if all barred quantities are replaced by final values at t^{n+1} and the tilde quantities are substituted by barred ones.

For typical cases, we have used values of N between 100 and 200 and from 1000 to 4000 time steps per cycle. Bubbles that behave nearly adiabatically need more internal nodes to resolve the boundary layer near the wall, and the number of time steps must be large at high amplitude, where the motion near radius minima is quite rapid. Empirically, we find a stability limit

$$\chi\Delta t/\Delta y^2 \lesssim 25.$$

The number in the right-hand side decreases somewhat at large amplitudes. We have also implemented a fourth-order Runge–Kutta integration scheme, but it was found to be less stable.

A good way to monitor the numerical error is to calculate, at each time step, the total mass m contained in the bubble from

$$m = 3pR^3\int_0^1\frac{y^2}{T(y)}dy. \tag{A21}$$

The nondimensionalization used here is such that $m = 1$ at equilibrium. For the results presented in this article, we have used enough time steps and nodes to ensure a maximum error in m less than 3%–4%. However, cases in which the error was as large as 7% did not show very large discrepancies from the more precise results.

[1]H. Pfriem, Akust. Zh. **5**, 202 (1940).
[2]C. Devin, J. Acoust. Soc. Am. **31**, 1654 (1959).
[3]A. Prosperetti, J. Acoust. Soc. Am. **61**, 17 (1977).

[4]M. Fanelli, A. Prosperetti, and M. Reali, Acustica **47**, 253 (1981).

[5]M. Minnaert, Phil. Mag. **16**, 235 (1933).

[6]B. E. Noltingk and E. A. Neppiras, Proc. R. Phys. Soc. London Ser. B **63**, 674 (1950).

[7]H. G. Flynn, "Physics of acoustic cavitation in liquids," in *Physical Acoustics*, edited by W. P. Mason (Academic, New York, 1964), Vol. 1, Part B, pp. 58–172.

[8]R. E. Apfel, J. Acoust. Soc. Am. **69**, 1624 (1981).

[9]W. Lauterborn, J. Acoust. Soc. Am. **59**, 283 (1976).

[10]Y. A. Akulichev, Sov. Phys. Acoust. **13**, 149 (1967).

[11]J. B. Keller and I. I. Kolodner, J. Appl. Phys. **27**, 1152 (1956).

[12]A. Prosperetti, J. Acoust. Soc. Am. **56**, 878 (1974).

[13]J. B. Keller and M. Miksis, J. Acoust. Soc. Am. **68**, 628 (1980).

[14]L. A. Crum and A. Prosperetti, J. Acoust. Soc. Am. **75**, 1910 (1984).

[15]W. Lauterborn and E. Suchla, Phys. Rev. Lett. **53**, 2304 (1984).

[16]H. G. Flynn, J. Acoust. Soc. Am. **57**, 1379 (1975).

[17]R. Hickling, J. Acoust. Soc. Am. **35**, 967 (1963).

[18]R. I. Nigmatulin and N. S. Khabeev, Fluid Dyn. USSR **12**, 867 (1977).

[19]F. B. Nagiev and N. S. Khabeev, Sov. Phys. Acoust. **25**, 148 (1979).

[20]R. I. Nigmatulin, N. S. Khabeev, and F. B. Nagiev, Int. J. Heat Mass Transfer **24**, 1033 (1981).

[21]M. Fanelli, A. Prosperetti, and M. Reali, Acustica **49**, 98 (1981).

[22]D. Y. Hsieh and M. S. Plesset, J. Acoust. Soc. Am. **33**, 206 (1961).

[23]A. I. Eller, J. Acoust. Soc. Am. **52**, 1447 (1972).

[24]L. A. Crum, J. Acoust. Soc. Am. **68**, 203 (1980).

[25]M. S. Plesset and A. Prosperetti, "Bubble dynamics and cavitation," Annu. Rev. Fluid Mech. **9**, 145 (1977).

[26]L. Trilling, J. Appl. Phys. **23**, 14 (1952).

[27]A. Prosperetti and A. Lezzi, J. Fluid Mech. **168**, 457 (1986).

[28]A. Prosperetti, Ultrasonics **22**, 69 (1984).

[29]A. Prosperetti, submitted to J. Fluid Mech.

[30]E. Cramer, "The dynamics and acoustic emission of bubbles driven by a sound field," in *Cavitation and Inhomogeneities in Underwater Acoustics*, edited by W. Lauterborn (Springer, New York, 1984), p. 54.

[31]K. Commander, "A theoretical investigation of acoustic cavitation," Ph. D. dissertation, University of Mississippi, Oxford, MS, 1985.

[32]A. Shima, S. C. Rajvanshi, and T. Tsujino, J. Acoust. Soc. Am. **77**, 1702 (1985).